A large-scale outdoor atmospheric simulation smog chamber for studying atmospheric photochemical processes: Characterization and preliminary application

Junling Li, Hong Li, Xuezhong Wang, Weigang Wang, Maofa Ge, Hao Zhang, Xin Zhang, Kun Li, Yan Chen, Zhenhai Wu, et al.

A Large-Scale Outdoor Atmospheric Simulation Smog Chamber for Studying Atmospheric Photochemical Processes: Characterization and Preliminary Application

Junling Li[1,2], Hong Li[*,1], Xuezhong Wang[1], Weigang Wang[3], Maofa Ge[3], Hao Zhang[1], Xin Zhang[1], Kun Li[4], Yan Chen[3], Zhenhai Wu[1], Fahe Chai[1], Fan Meng[1], Yujing Mu[5], Abdelwahid Mellouki[6], Fang Bi[1], Yujie Zhang[1], Lingyan Wu[2], Yongchun Liu[7]

1. State Key Laboratory of Environmental Criteria and Risk Assessment, Chinese Research Academy of Environmental Sciences, Beijing 100012, China. E-mail: lijl@craes.org.cn
2. Key Laboratory of Atmospheric Chemistry , China Meteorological Administration, Beijing 100081, China
3. State Key Laboratory for Structural Chemistry of Unstable and Stable Species, Beijing National Laboratory for Molecular Sciences (BNLMS), CAS Research/Education Center for Excellence in Molecular Sciences, Institute of Chemistry, Chinese Academy of Sciences, Beijing 100190, China
4. Laboratory of Atmospheric Chemistry, Paul Scherrer Institute (PSI), 5232 Villigen, Switzerland
5. Research Centre for Eco-Environmental Sciences, Chinese Academy of Sciences, Beijing 100085, China
6. Institut de Combustion Aérothermique, Réactivité et Environnement, Centre National de la Recherche Scientifique (ICARE-CNRS), Observatoire des Sciences de l'Univers en région Centre (OSUC), CS 50060, 45071 cedex02 Orléans, France
7. Beijing Advanced Innovation Center for Soft Matter Science and Engineering, Beijing University of Chemical Technology, Beijing 100029, China

Abstract: Understanding the formation mechanisms of secondary air pollution is very important for the formulation of air pollution control countermeasures in China. Thus,

a large-scale outdoor atmospheric simulation smog chamber was constructed at Chinese Research Academy of Environmental Sciences (the CRAES Chamber), which was designed for simulating the atmospheric photochemical processes under the conditions close to the real atmospheric environment. The chamber consisted of a 56 m^3 fluorinated ethylene propylene (FEP) Teflon film reactor, an electrically-driven stainless steel alloy shield, an auxiliary system, and multiple detection instrumentations. By performing a series of characterization experiments, we obtained basic parameters of the CRAES chamber, such as the mixing ability, the background reactivity, and the wall loss rates of gaseous compounds (propene, NO, NO_2, ozone) and aerosols (ammonium sulfate). Oxidation experiments were also performed to study the formation of ozone and secondary organic aerosol (SOA), including α-pinene ozonolysis, propene and 1,3,5-trimethylbenzene photooxidation. Temperature and seed effects on the vapor wall loss and SOA yields were obtained in this work: higher temperature and the presence of seed could reduce the vapor wall loss; SOA yield was found to depend inversely on temperature, and the presence of seed could increase SOA yield. The seed was suggested to be used in the chamber to reduce the interaction between the gas phase and chamber walls. The results above showed that the CRAES chamber was reliable and could meet the demands for investigating tropospheric chemistry.

Keywords:

Outdoor smog chamber

Characterization experiments

Photooxidation reactions

Secondary organic aerosol

---

* Corresponding author. E-mail: lihong@craes.org.cn (Hong Li)

Introduction

Air pollution has been one of the most important global environmental issues in the past few decades, which is related to human health, ecological environment, and climate

change (Guo et al., 2014; Huang et al., 2014; Menon et al., 2002; Zhang et al., 2016). To study the chemical processes of atmospheric pollution, many smog chambers had been developed worldwide. Smog chambers were initially constructed for developing and evaluating atmospheric gas-phase chemical mechanisms, generating and validating computer models of the chemistry occurring in polluted atmosphere (Akimoto et al., 1979a; CARTER et al., 1982a). Now the smog chambers could be used to study the formation and evolution of specific pollutants in the atmosphere by controlling or restricting certain meteorological conditions and reactant compositions, and could also be applied to obtain kinetic parameters of specific reactants (Knox, 1965; Li et al., 2017a; Li et al., 2017b; McFiggans et al., 2019; Yu et al., 1997; Zhou et al., 2019).

According to the light sources adopted, the smog chambers were usually divided to be indoor chamber and outdoor chamber; indoor chambers were equipped with artificial light sources while outdoor chambers benefitted from natural solar radiation (Seakins, 2010). For indoor chambers, ultraviolet lamps were used to simulate natural solar radiation, thus the spectral distribution was not exactly the same as the tropospheric sunlight spectrum, which made the simulation results might deviate from that in nature. However, it is relatively easier to control the experimental conditions for the indoor chambers, various experimental conditions (e.g. temperature, relative humidity, pressure) could be precisely designed for different experimental purposes, which means that the repeatability of experimental results could be ensured under precise control of the reaction conditions. In comparison, since outdoor chambers usually had larger size, there are relative smaller surface to volume ratio for outdoor chamber, which could minimize the wall effects and wall loss of gaseous species and particles. The experiments inside the outdoor chambers were performed at ambient temperature and pressure, and also with natural solar radiation. Hence, the outdoor chamber was an ideal reactor to simulate the atmospheric photochemical processes. However, the drawbacks of the outdoor smog chamber were that the temperature, humidity, and solar flux varied gradually during the experimental period, and it was almost impossible to guarantee reproducible irradiation from day to day. (Johnson et al., 2004; Karl et al., 2004; Seakins, 2010).

Many outdoor and indoor chambers had been established and applied to simulate the atmospheric photochemical processes worldwide (Table S1). The construction of large-size smog chamber abroad began in the 1970s, when the starting point was to study near-ground ozone pollution (Akimoto et al., 1979b; Carter et al., 1982b). In the

following thirty years, indoor and outdoor chambers were widely used to study the generation mechanism of secondary pollutants, such as ground-level-ozone (Dodge, 2000; Hess et al., 1992; Simonaitis et al., 1997) and SOA (Griffin et al., 1999; Leone et al., 1985; Martian-Reviejo and Wirtz, 2005; McMurry and Grosjean, 1985; Odum et al., 1996; Paulsen et al., 2005a; Saathoff et al., 2009). After the 1980s, many large smog chambers have been transformed, rebuilt, and upgraded, to deal with the emerging scientific issues of atmospheric environment and atmospheric chemistry, such as $PM_{2.5}$ pollution (Hallquist et al., 2009; Hurley et al., 2001; Johnson et al., 2004), intermediate products of VOCs reaction (Bloss et al., 2005; Bohn et al., 2005; Brauers et al., 2003; Ren et al., 2017), multiphase reactions (Poschl and Shiraiwa, 2015; Warneke et al., 2004), reaction kinetic parameters (Karl et al., 2004; Ren et al., 2019; Rohrer et al., 2005), etc.

The domestic experimental research with the smog chamber started in the early 1980s, later than abroad. Peking University built the earliest indoor photochemical smog chamber in 1982, in response to the photochemical smog phenomenon that occurred in Lanzhou (Tang et al., 1982). A series of photochemical simulation experiments of hydrocarbons and NO_x were designed and conducted according to the atmospheric conditions in Lanzhou and Beijing (Zhang and Li, 1998). Then a serious environmental issues were studied based on the smog chambers constructed with various size in the past decades, including the mechanism of photochemical reaction (Liu et al., 2017; Wang et al., 2014; Wu et al., 2007), ozone and SOA formation (Li et al., 2018a; Ma et al., 2018; Wang et al., 2015), biomass burning reactions (Zhang et al., 2011), the photochemical process of the gasoline and diesel (Chen et al., 2019a; Chen et al., 2019b; Kamens et al., 2011), physicochemical properties of SOA formed under various conditions (Li et al., 2017a; Li et al., 2020; Li et al., 2018b; Peng et al., 2018; Zhang et al., 2020), et al. However, most of the chambers constructed in China were indoor smog chambers, establishment large-scale outdoor smog chambers in China was limited. In order to study the atmospheric pollution process close to China's actual atmospheric environment, it was necessary to build a large outdoor smog chamber in China.

This work described a new outdoor photochemical smog chamber constructed at the Chinese Research Academy of Environmental Sciences (the CRAES chamber). As the large-scale outdoor smog chamber in China at present, it was designed to simulate the atmospheric photochemical processes at ambient temperature and radiation. A

series of characterization experiments were performed, including the light-transmission rate of the Teflon reactor, the mixing ability, the wall loss of gaseous pollutants and particles, and the blank photochemical background. We had also performed preliminary applications of the smog chamber, including the classic gas-phase photochemical reaction of propene, the yield of SOA derived from α-pinene ozonolysis and 1,3,5-trimethylbenzene photochemical reaction. The temperature and seed effects on vapor wall loss and SOA yield were investigated in this work.

1. Facility

The CRAES chamber was located on the rooftop of atmospheric photochemical smog chamber simulation laboratory building (40°02'27.73'N, 116°24'41.56'E), aligning in north-south direction. The chamber was mainly composed of a Teflon reactor, an enclosure, an auxiliary system and a detection system. Its schematic was illustrated in **Fig. 1**, and the pictures of the reactor and enclosure were shown in **Fig. S1**.

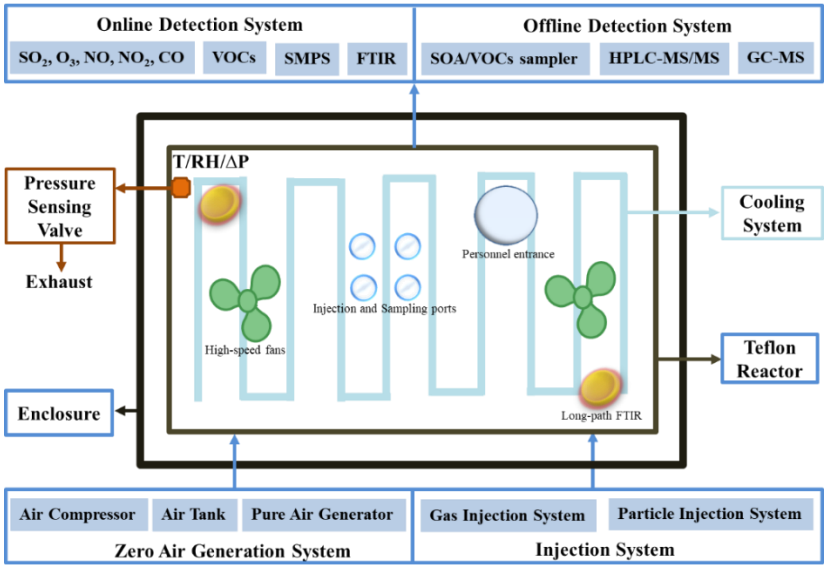

Fig. 1. Schematic diagram of the CRAES chamber.

The frame of the reactor was made of aluminum alloy, of which the bottom was made of aluminum supported by steel structure. As shown in **Fig. S1**, injection and sampling ports, air purification system import and export, and port for personnel in and out (staged manual cleaning the walls inside the chamber) were located on the bottom of the frame by using the flanges. All the connection parts on the bottom of the reactor were made of Teflon or stainless steel (covered with Teflon film) without O-rings to

avoid the evaporation of the organic impurities into the reactor. The reactor walls were made of 0.1 mm fluorinated ethylene propylene (FEP) Teflon film (FEP 100，DuPont USA), and it was suspended on the frame. The volume of the reactor was 56 m^3 (3.2 m × 6.2 m × 2.5 m), with a surface to volume ratio approximately 1.55 m^{-1}.

The enclosure consisted of a shield and an electrical control system. The main body of the shield was made of stainless steel supported by a full steel frame and had a rectangular parallelepiped shape. This shield could protect the reactor against adverse weather conditions. The opening and closing of the shield was achieved by an electrical control system. The entire system was equipped with an emergency stop device to deal with sudden failures and ensured that the enclosure and Teflon reactor was not damaged.

The cooling system consisted of a condensing compressor (Industrial Chiller，ANGES, China) and a condensing tube. The tube connected with the condensing compressor being evenly distributed below the steel plate at the bottom of the reactor. The water-cooling method ensured that the temperature of the reactor was within a controllable range, especially under high temperature condition in summer.

The zero air generation system consisted of two air compressors, two air tank and two AADCO pure air generators (Model 737, AADCO Instruments Inc., USA). The NO, NO_2, ozone, NH_3, non-methane hydrocarbons (NMHC) (< 1 ppb, volume fraction), and particles in the purified air were below detection limit, and the relative humidity (RH) was less than 1%. The maximum flow rate of the purified air was 245±5 L/min. The purified air was used as the matrix air and carrier gas. All gas lines of the system were made of stainless steel or Teflon. Gaseous species were injected into the reactor through Teflon lines by cylinders connected with pressure reducing values and mass flow controllers. Most gaseous species were commercial cylinder gases, and there were also gaseous species that were configured according to the experimental requirements.

Instrumentations of the CRAES chamber were summarized in **Table 1**. The intensity of the UVA and UVB was monitored by meteorological ecological environment monitoring system (Jinzhou Sunshine Technology Co. Ltd. China). Airmo VOC online analyzer (GC-866, Chromato-sud, France) was used to detect the parent VOCs concentrations in the chamber. Its detection limit was less than 1.0 ppb. The

VOCs concentrations were also monitored by a gas chromatography mass spectrometer (GC-MS, 7890A/5975C, Agilent) coupled with a model 7100 preconcentrator (Entech Instruments Inc., USA). The formed aldehyde and ketone were collected by a custom-made Aldehyde Ketone Sampler, and then the samples were analyzed by a high performance liquid chromatography-UV detector-mass spectrometry (HPLC-UV-MS; SHIMADZU, Japan, LC20AD/SPD-20A; ABSCIEX, USA, API 3200). The aerosols formed in the chamber were collected by a low flow sampler (LV 40BW, Sibata Scientific Technology Ltd., Soka, Japan) with a sample speed of 5 L/min. High performance liquid chromatography mass spectrometry (HPLC-MS, SHIMADZU, LC20A; ABsciex API3200) and high resolution electrospray ionization time-of-flight mass spectrometry (ESI-TOF-MS, micrOTOF Ⅱ, Bruker) were used to detect the chemical composition of the formed aerosols. The aerosol particle size distribution was detected by a scanning mobility particle sizer (SMPS), which composed of an electrostatic classifier (EC, Model 3080, TSI Inc., USA), a differential mobility analyzer (DMA, Model 3081, TSI Inc., USA) and a condensation particle counter (CPC, Model 3772, TSI Inc., USA). The flow rates of sheath and aerosol flow were set to 3.0 and 0.3 L/min, respectively, allowing for a size distribution scan ranging from 15.1 to 661.2 nm within 120 s. The aerosol particles were also monitored by a nano-scanning mobility particle sizer (nano-SMPS, TSI3938E57), which was composed of an electrostatic classifier (EC, Model 3082, TSI Inc., USA), a differential mobility analyzer (DMA, Model 3086, TSI Inc., USA), a Nano Enhancer (Model 3757), and a condensation particle counter (CPC, Model 3750, TSI Inc., USA). The flow rates of sheath and aerosol flow were set to 25 and 2.5 L/min, respectively, allowing for a size distribution scan ranging from 1 to 30.5 nm within 60 s. The temperature and relative humidity inside the chamber were monitored by industrial temperature and humidity transmitter (CWS16, CCY11, Beijing Star Sensor Technology Co., LTD. China).

Table 1. Overview of Instruments of the CRAES Chamber.

Instrument	Manufacturer	Measured Parameters	Accuracy
SO_2 analyzer	EC 9850, ECOTECH, Australia	SO_2 concentration	0.5 ppb
O_3 analyzer	EC 9830, ECOTECH, Australia	O_3 concentration	0.5 ppb

NO_x analyzer	EC 9841, ECOTECH, Australia	NO_X concentration	0.5 ppb
CO analyzer	EC 9810, ECOTECH, Australia	CO concentration	50 ppb
AirmoVOC online analyzer	GC-866, Chromato-sud, France	VOC concentrations	＜1.0 ppb
Long-path FTIR	NICOLET6700, Thermofisher, USA	Infrared absorption spectrum	0.09 cm^{-1}
Aldehyde Ketone Sampler	Custom-made	Collect the aldehyde and ketone	40 ppb
SMPS	TSI Inc. USA	Particle size distribution (15-660 nm)	± 10%
nano-SMPS	TSI Inc. USA	Particle size distribution (1-30.5 nm)	± 10%
Low Flow Sampler	LV 40BW, Sibata Scientific Technology Ltd., Soka, Japan	Collect the aerosol particles	--
HPLC-UV-MS	LC20AD/SPD-20A, SHIMADZU, Japan; API 3200, ABSCIEX, USA	Chemical compositions of the aerosols	1.0 ppt
Industrial Transmitter	Beijing Star Sensor Technology Co., LTD.	Temperature, Relative Humidity, Differential Pressure	--
Meteorological Ecological Environment Monitoring System	Jinzhou Sunshine Technology Co. Ltd	UVA, UVB	--
$J(NO_2)$ filter radiometer	METCON, Germany	photolysis rate of NO_2 (280~420nm)	1.5×10^{-6} sec^{-1}/mV

2. Characterization Experiments

In order to verify the smog chamber's utility, a series of characterization experiments were performed, including the light transmission of the Teflon film, the mixing ability, the background experiments (zero air, zero air +NO_x), and wall losses of gaseous pollutants and particles.

2.1 Light Transmission

The light densities of the solar radiation before and after the Teflon film were detected by an irradiation spectrometer (Jaz spectral sensing suite, Ocean Optics Inc., USA), and then the light transmission of the new Teflon film was calculated.

Fig. 2 showed the transmission rate of the full solar spectrum for the Teflon film. The transmission rate was above 90% at the wavelength range of 350-900 nm. The solar radiation spectra were almost identical before and after the film, which showed that this film was suitable for the Teflon reactor of the smog chamber.

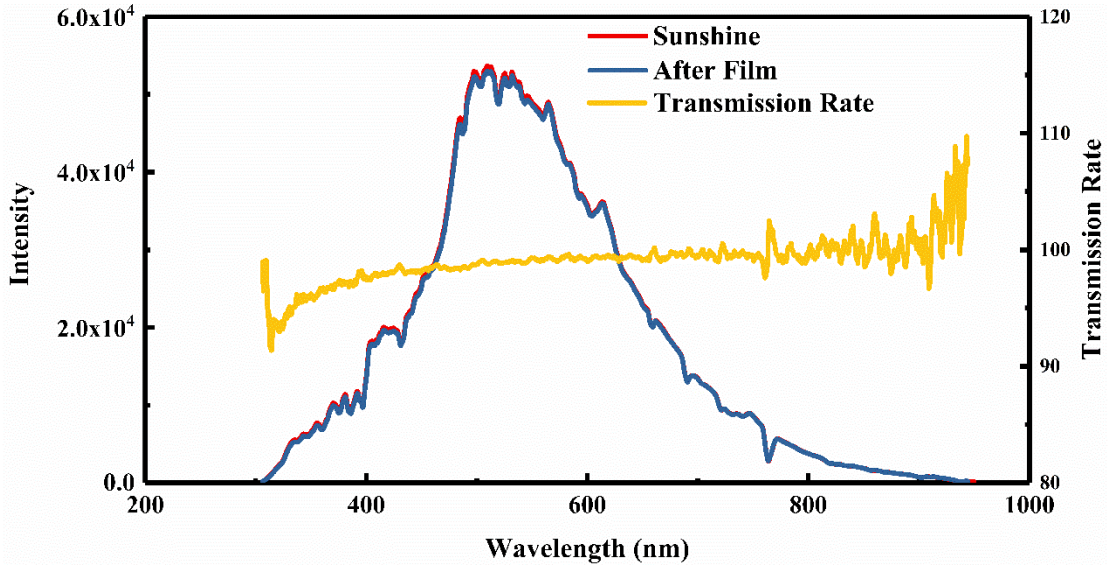

Fig. 2. Ultraviolet-visible transmission spectra of the Teflon film.

The light transmission of this chamber were also detected by comparing the NO_2 photolysis rate inside and outside the chamber. The NO_2 photolysis rate inside the chamber was estimated by steady-state actinometry (Wang et al., 2015). NO_2 was injected into the chamber and irradiated, and the resulting ozone, NO_2, and NO mixing ratios were measured. The photolysis rate constant, $J(NO_2)$, was then estimated as the following equation:

$$J = k_1[O_3][NO]/[NO_2] \quad (1)$$

where k_1 (cm^3/molecule/sec) was the rate constant of NO and ozone reaction. The measured $J(NO_2)$ inside the chamber was compared to the NO_2 photolysis rate outside the chamber, and the results were shown in **Fig. 3.** Results showed that the NO_2 photolysis rate inside the chamber was close to that of natural sunlight.

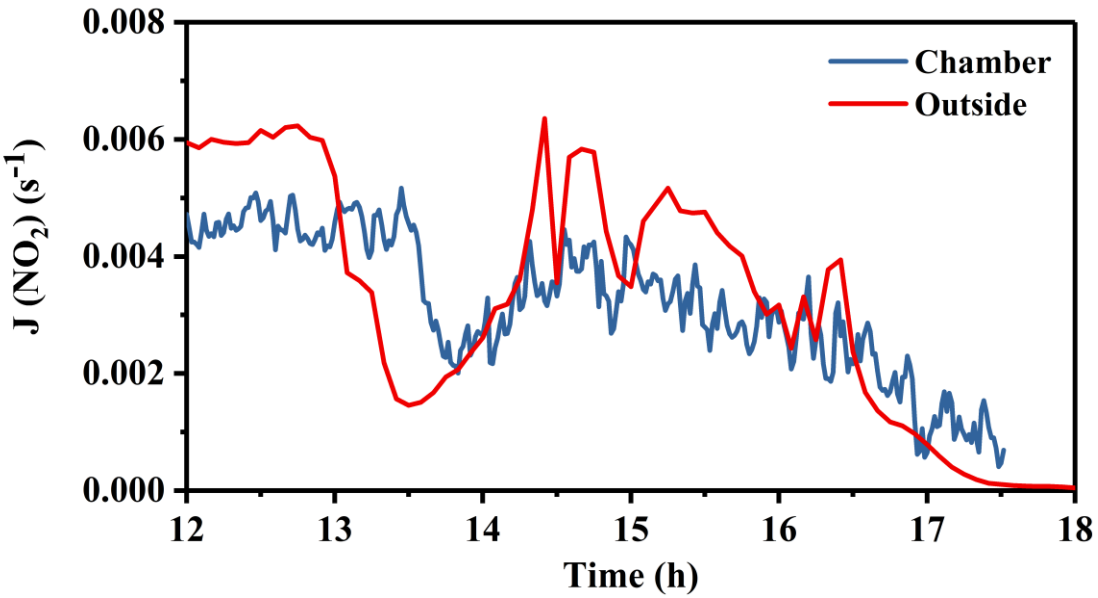

Fig. 3. The NO_2 photolysis rate inside and outside the chamber.

2.2 Mixing Ability

The mixing ability of the chamber was characterized by the length of time when the gas concentration got stable. Generally, the shorter mixing time referred to the better mixing ability of the chamber. Carbon monoxide (CO) was used as the tracer to detect the mixing ability of gaseous species inside the chamber. A known volume of CO gas was injected into the chamber by cylinder. The injection line was located in the middle of the chamber. Three high-speed fans were placed at the opposite corner of the chamber: one bracket was equipped with a vertical blown fan, and one bracket was equipped with two horizontal blown fans. The brackets supporting the fans were all covered with Teflon films. The CO concentration was measured by an EC 9810 CO analyzer (ECOTECH, Australia) with a detection limit of 50 ppb.

As revealed by **Fig. 4**, the CO gas entering the chamber could be mixed evenly within four min for the four injections. The mixing time was very short compared to the entire experimental process (usually several hours). This showed the good mixing ability of the chamber for experiments.

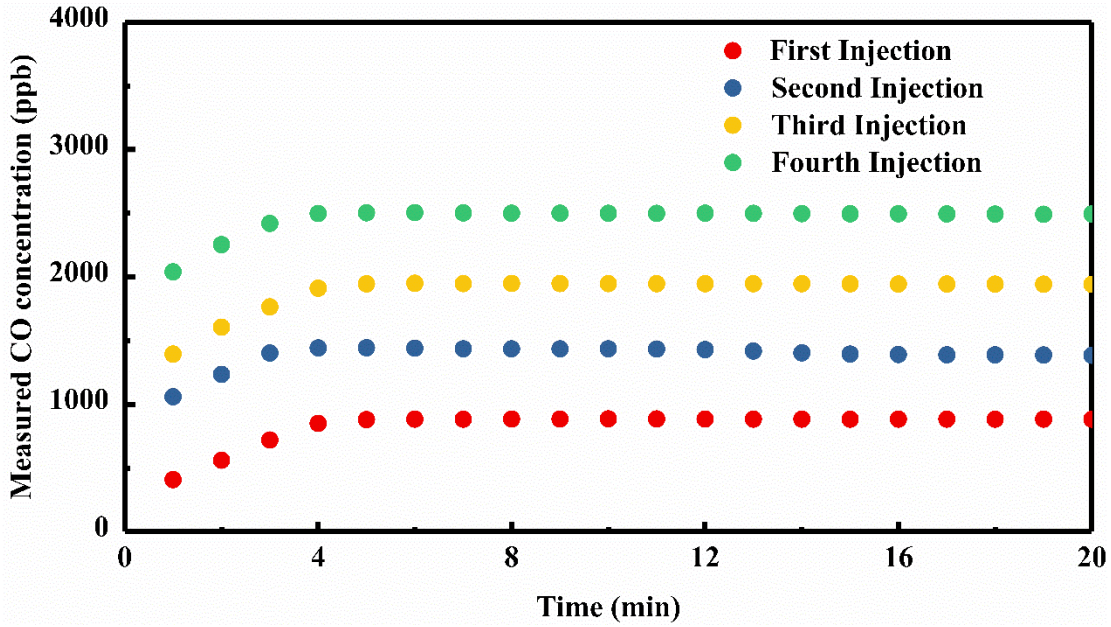

Fig. 4. Measured carbon monoxide concentration as a function of time in four injections.

3. Preliminary Application Experiments

3.1 Background Experiments

In order to minimize the existence of organic impurities desorbing from Teflon films (Kelly, 1982), the newly-made reactor was exposed to sunlight for 10 hours with zero air containing 1.5-2 ppm of ozone. Then the chamber was flushed for 24 hours with zero air. After the above protocols, the chamber filled with zero air was kept in the dark for more than 12 hours, and no measurable organic impurities was detected by the Airmo VOC online analyzer. Then the chamber filled with zero air or zero air + NO_X was exposed to sunlight for 8 hours. The concentrations of ozone, NO, and NO_2 were measured by EC 9830 ozone analyzer and EC 9841 NOx analyzer (Ecotech, Australia). The detection limit of ozone and NOx were both 0.5 ppb. The aerosol particle size distribution was detected by a SMPS.

The gas analyzers above were calibrated weekly by gas dilution calibration system (4010 Gas Dilution Calibrator and Model 1001 Zero Air Source, Sabio) with certified cylinders of gases. The NO, NO_2 and CO gases ($\geq$ 99%) were commercially available, and they were used without further purification. Ozone was generated by a commercial ozone generator (VMUS-4, Azco Industries Ltd, Canada), which connected the oxygen cylinder through the Teflon tube. The concentration of generated ozone could be

estimated based on the oxygen flow rate and time through the ozone generator.

Fig. 5a and b showed the concentration of NO, NO_2, ozone and mass of formed particles for background experiments with only zero air. NO concentration was in the range of 0-1 ppb with no detectable increase, while NO_2 was in the range of 0-2 ppb with a slightly increasing trend, which was probably due to the release from the Teflon films. Concentration of ozone increased slowly with the sunlight irradiation, up to 21 ppb. This was likely due to the irradiation of the purified matrix air, and was consistent with the previous reported data (Grosjean, 1985). As shown in Fig 4b, the formation of particles was negligible (less than 0.01μg m^{-3}).

The chamber filled with zero air and 71 ppb NOx was exposed to sunlight irradiation for 8 hours. As shown in **Fig. 5c and d**, concentration of NO_x slightly decreased as the illumination time increases, while ozone concentration increased and reached 32 ppb when the chamber was closed. After 4 h of sunlight irradiation, a small amount of particles was formed, which might be from the reaction of OH radicals (from NOx cycles) with organic impurities desorbed from the Teflon films. However, the particle mass concentration here (< 0.1μg m^{-3}) was much less than the particles produced by reactions of volatile organic compounds discussed below.

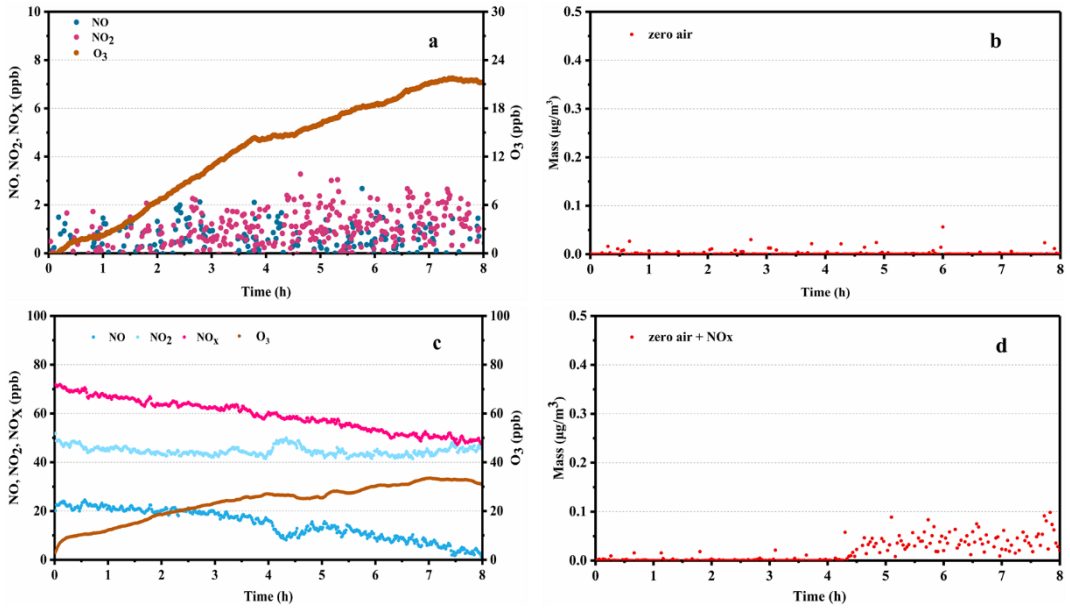

Fig. 5. NO, NO_2, NO_x, and ozone concentration as a function of sunlight irradiation time with zero air (a) and with zero air + NO_x (c); Mass concentration of formed particles as a function of sunlight irradiation time with zero air (b) and with zero air + NO_X (d).

3.2 Wall Loss of Gaseous Pollutants

In the CRAES chamber, the wall loss of propene, NO, NO_2, and ozone were evaluated by injecting the gases into the chamber and monitoring their decay with duration of more than 8 hours in the dark. The wall loss rates of the gaseous pollutants were obtained by treating the gas wall losses as first order process. The temperature and relative humidity conditions during the measurement processes were 20-29 ℃ and less than 7%, respectively. All wall loss experiments were performed with initial concentration ranging from 80 ppb to 400 ppb.

As shown in **Table 2**, the wall loss rates of NO, NO_2, ozone and propene were 0.65×10^{-4} min^{-1}, 1.01×10^{-4} min^{-1}, 2.65×10^{-4} min^{-1}, and 0.09×10^{-4} min^{-1}, respectively. The wall loss rates of interested gaseous species were all within the value ranges of previous data for chambers facilities constructed from Teflon films(Bloss et al., 2005; Grosjean, 1985; Metzger et al., 2008; Wang et al., 2015; Wang et al., 2014). For the relative high wall loss rate of ozone, it might indicate the permeability of the film, and ozone might react with the reactive compounds for its high reactivity. While for propene, its wall loss rate was nearly negligible, which was consistent with the reported values: for GIG-CAS (Wang et al., 2014) smog chamber, no wall loss was detected; Wu et al. (2007) calculated the wall loss rate as 0.066×10^{-4} min^{-1} in a 2 m^3 Teflon smog chamber; and for ICCAS (Wang et al., 2015) smog chamber, the wall loss rates were (0.30-0.31) $\times 10^{-4}$ min^{-1}, respectively.

Table 2. Summary of wall loss rates of gaseous pollutants in CRAES smog chamber and comparison with other chamber facilities.

Species	Wall Loss Rate ($\times10^{-4}$ min^{-1})						
	CRAES	GIG-CAS[a]	ERT[b]	EUPHORE[c]	ICCAS[d]		PSI[e]
	56 m^3	30 m^3	80 m^3	200 m^3	5×2 m^3		27 m^3
					right	left	
C_3H_6	0.09	ND[f]	NA[g]	NA	0.31	0.3	NA
O_3	2.65	1.31±0.24	1.3±0.9	1.8	3.1	2.5	1.2-4.8
NO	0.65	1.41±0.40	0-2.0	NA	3.1	3.0	NA
NO_2	1.01	1.39±0.68	0-8.2	NA	4.5	3.8	0.13-2.52

a: Wang et al. (2014); b: Grosjean (1985); c: Bloss et al. (2005); d: Wang et al. (2015); e: Metzger

et al. (2008); f: Not detectable; g: Not applicable

3.3 Wall Loss of Particles

The particles inside the chamber could deposit on the chamber walls with the result of turbulent, Brownian diffusion, gravitational sedimentation as a function of the particle size. The wall loss rates of particles were obtained by treating the wall loss as a first-order process, and the particle loss coefficient K_{dep} could be expressed as following equation:

$$\frac{d_{N(dp)}}{d_t} = -K_{dep}(d_p)N(d_p) \quad (2)$$

where *N(dp)* was the number concentration of the particles, and K_{dep} *(*d_p*)* was the loss coefficient of particles in the diameter d_p.

Ammonium sulfate particles were used as a reference aerosol to measure the particle wall losses. Ammonium sulfate solution was atomized with an atomizer (TSI, Model 3079A, TSI Inc., USA), then the formed particles were passed through a diffusion dryer and a neutralizer (Model 3088, TSI Inc., USA) before introducing into the reactor.

The wall loss rate of ammonium sulfate was shown in **Table 3** and **Fig. 6.** As shown in **Table 3**, the overall number wall loss rate K_{dep} was 0.23 h^{-1}, which leaded to a lifetime of 4.4 h for particles. While for particles in the diameter range from 100 to 600 nm, as shown in **Fig. 6b,** K_{dep} were determined to be in the range of 0.186-0.30 h^{-1}. The relationship between K_{dep} and d_p was determined by optimization of four parameters (*a*, *b*, *c*, *d*) in the following equation:

$$K_{dep}(d_p) = ad_p^b + \frac{c}{d_p^d} \quad (3)$$

where parameters *a*, *b*, *c* and *d* were optimized to be 6.34718×10^{-6}, 1.55745, 6.38387, and 0.66596, respectively.

As shown in **Table 3**, the wall loss rate for the particles in different chambers were various, this might due to the different environmental conditions insider the chamber facilities. In addition, the relationship between K_{dep} and d_p of an aerosol in a cubic vessel were theoretically expressed by Corner and Pendlebury (1951), gravitational settling and diffusion are considered:

$$K_{dep} = \frac{1}{100}\left[\frac{6\sqrt{K_e D}}{\pi} + V\ coth\frac{V\pi}{4\sqrt{K_e D}}\right] \quad (4)$$

where D, K_e, and V were the Brownian diffusivity, a constant for eddy diffusion, and the terminal settling velocity, respectively.

As mentioned above, two high-speed fans were located insider the chamber, which would affect the eddy diffusion and vibrate the wall of the chamber. The eddy diffusion and vibration of the chamber wall were likely to affect the deposition of the aerosol inside the chamber. For the experiments performed in this smog chamber in future, in order to reduce the loss of particles, the fans will be turned off after the precursors are evenly mixed.

Table 3. Summary of wall loss rates of particles in CRAES smog chamber and comparison with other chamber facilities.

Chamber	Volume (m^3)	Chamber Materials	Wall Loss Rate (h^{-1})	Particle Life Time (h)	References
CRAES	56	FEP	0.23	4.4	This work
GIG-CAS	30	FEP	0.17	5.9	Wang et al. (2014)
PSI	27	FEP	0.21	4.8	Paulsen et al. (2005b)
EUPHORE	200	FEP	0.18	5.6	Martian-Reviejo and Wirtz (2005)
ICCAS	5×2	FEP	0.12-0.26	3.8-8.3	Wang et al. (2015)
SAPHIR	270	FEP	0.27	3.7	Rollins et al. (2009)
CMU	12	FEP	0.40	2.5	Donahue et al. (2012)

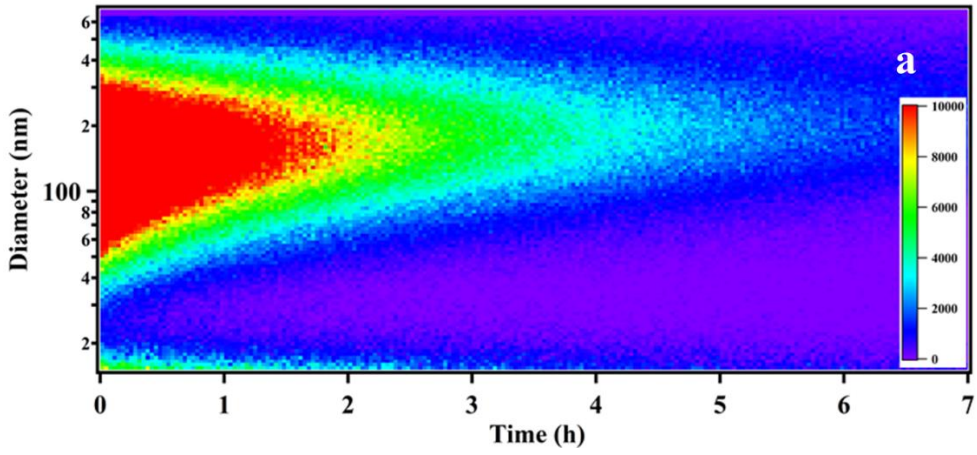

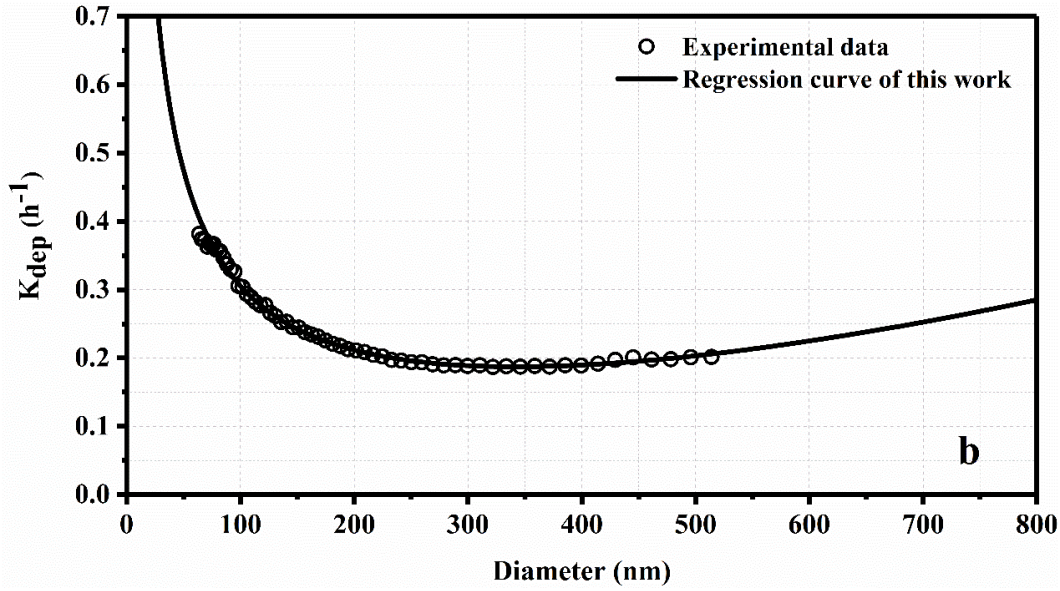

Fig. 6. (a) Number concentration of ammonium sulfate particles as a function of time after its introduction into the chamber, the color map refers to the number concentration of the particles (#/cm^3). (b) Particle wall loss rate constants for different particle diameter sizes.

3.4 Preliminary Application Experiments

On the basis of characterization experiments, we carried out a series of preliminary applications experiments with the CRAES chamber, including photochemical reactions of propene-NOx, SOA yields derived from α-pinene ozonolysis and 1,3,5-trimethylbenzene (1,3,5-TMB)-NO_x photo-oxidation.

3.4.1 Propene-NO_x Experiments

The propene-NO_x experiments were widely used to evaluate the ability of the smog chamber to test the chemical mechanisms (Wang et al., 2015; Wang et al., 2014). The propene-NO_x experiment was performed in the chamber close to real atmosphere. The initial concentration of propene, NO, NO_2, and ozone were 83, 9, 120, and 2 ppb, respectively. And the HONO concentration was 8 ppb. The photolysis rate of NO_2 was measured with *J(NO_2)* filter radiometer (METCON, Germany). The chemical mechanism of propene from the Master Chemical Mechanism (MCM) version 3.3.1 was applied to simulate the propene oxidation, which was operated with Facsimile. The experiments were compared with the simulation results.

Fig. 7 showed the concentration-time profiles of monitored and simulated propene, NO, NO_2, and ozone in propene-NO_x experiment. The wall loss rates of propene, NO,

NO_2, and ozone obtained in Sect 3.4 were added in the model. As revealed in **Fig. 7**, good agreements were obtained for propene, NO, and NO_2, while the concentration of ozone was little over-predicted, which was also observed by previous studies, e.g., Zador et al. (2005), Metzger et al. (2008), and Bloss et al. (2005). The results above showed that this chamber can provide valid data for gas-phase photochemical mechanism.

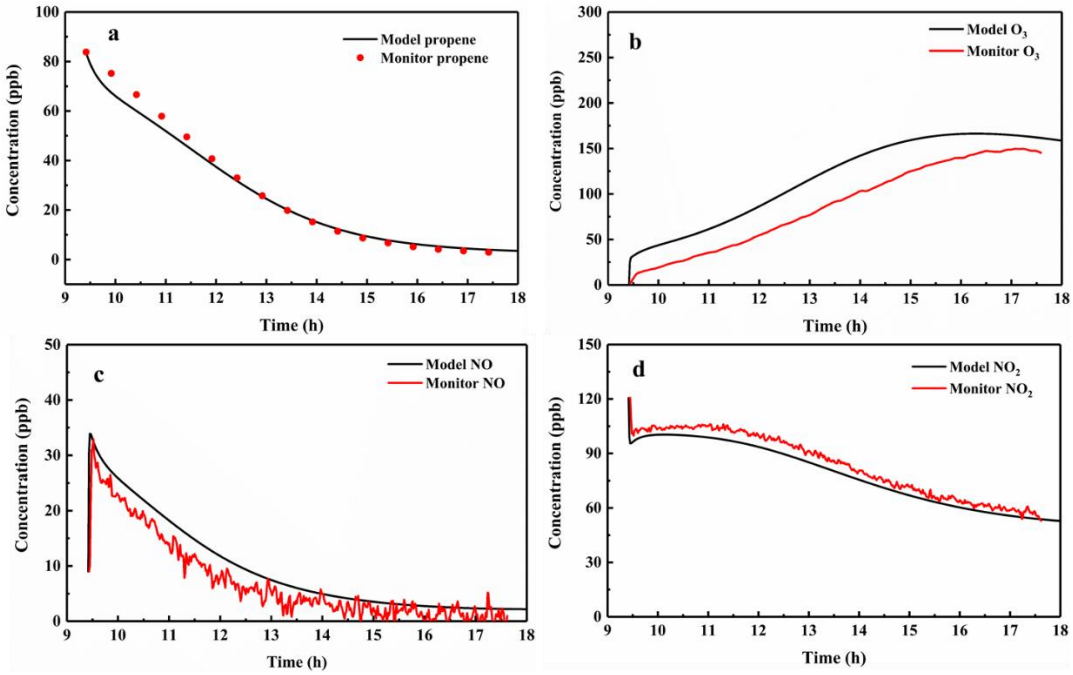

Fig. 7. Concentration-time profiles of monitored and simulated (a) propene, (b) ozone, (c) NO, and (d) NO_2 in the propene-NO_x experiment.

3.4.2 SOA Yields

A series of α-pinene ozonolysis and 1,3,5-trimethylbenzene (1,3,5-TMB)-NO_x photochemical experiments were carried in the CRAES chamber to verify its performance in studying the formation of SOA. Temperature and seed effect on the SOA yields were also investigated. All these experiments were carried out under dry conditions.

The aerosol yield *Y* was defined as the fraction of a reactive organic gas (*ROG*) that was converted to aerosol, which was calculated by the following equation(Odum et al., 1996):

$$Y = \frac{\Delta M_o}{\Delta ROG} \quad (5)$$

where ΔM_o was the aerosol mass concentration ($\mu g/m^3$) produced from a given amount of *ROG*, and ΔROG was the mass concentration ($\mu g/m^3$) of reacted precursor.

The two-product model was applied to simulate the SOA yield formed in the chamber, and it was calculated based on the following equation(Odum et al., 1996) (Odum et al., 1996):

$$Y = \sum_i Y_i = M_o \sum_i \left(\frac{\alpha_i K_{om,i}}{1+K_{om,i} M_o} \right) = M_o \left(\frac{\alpha_1 K_{om,1}}{1+K_{om,1} M_o} + \frac{\alpha_2 K_{om,2}}{1+K_{om,2} M_o} \right) \quad (6)$$

where Y_i was the yield of one individual product, α_i was the proportionality constant basing on the total concentration of product i, $K_{om,i}$ was the partitioning coefficient basing on the organic mass concentration of species i, M_o was the overall aerosol mass concentration.

The SOA yield was the result after particle and vapor wall loss correction. The correction coefficient of the particle wall loss was calculated based on the loss after the SOA mass reaches the maximum value. The details of the vapor wall loss of this chamber were introduced in the Supporting Information. Briefly, as shown in **Table S2**, both the temperature and seed could affect the vapor wall loss, the presence of seed in the reaction system could decrease the vapor wall loss, and the increase of temperature of the reaction system could decrease the vapor wall loss. Meanwhile, the vapor wall loss of different reaction systems was also different.

3.4.2.1 α-pinene ozonolysis experiments

Four α-pinene ozonolysis experiments were performed under dry conditions. The aerosol density was assumed to be 1 g/cm^3, which was referred to the literature values (Wang et al., 2014; Wirtz and Martin-Reviejo, 2003). The details of the experimental conditions were shown in **Table 4**.

The SOA yields of α-pinene ozonolysis was underestimated by a factor of 0.32−0.78 fold when considering vapor wall loss. After considering the vapor and particle wall loss, the optimal parameters α_1, α_2, $K_{om,1}$, and $K_{om,2}$ of this work were 0.3643, 0.4590, 0.0674, and 0.0006, respectively. The yield curve fitted well with the experiments data. SOA yields of α-pinene ozonolysis experiments of this work and data from other chamber facilities were shown in **Fig. 8**. The experiments in this work were

423 performed under low temperature (4.4-11.7℃), and the yields were comparable with the
424 yield data obtained under similar temperature condition (9.9-10.9 ℃) (Saathoff et al.,
425 2009). Meanwhile, according to the yield values reported in other previous studies (the
426 temperature conditions were higher than this work) (Cocker et al., 2001; Griffin et al.,
427 1999; Hoffmann et al., 1997; Saathoff et al., 2009; Wang et al., 2015), it could be seen
428 that temperature had important influence on the SOA yield, that a decrease in
429 temperature could enhance the SOA yield

430 **Table 4.** Experimental conditions and resulting SOA data of the α-pinene ozonolysis
431 experiments.

Date	Initial VOC (ppb)	Initial O_3 (ppb)	M_o ($\mu g/m^3$)	Temp. (℃)	SOA yield (%)
2019.12.11	394	500	841	4.4-8.8	51.83
2019.12.13	250	390	414	6.6-11.7	44.72
2019.12.16	175	307	210	6.2-6.8	39.46
2019.12.18	95	370	73	4.7-8.6	32.31

432

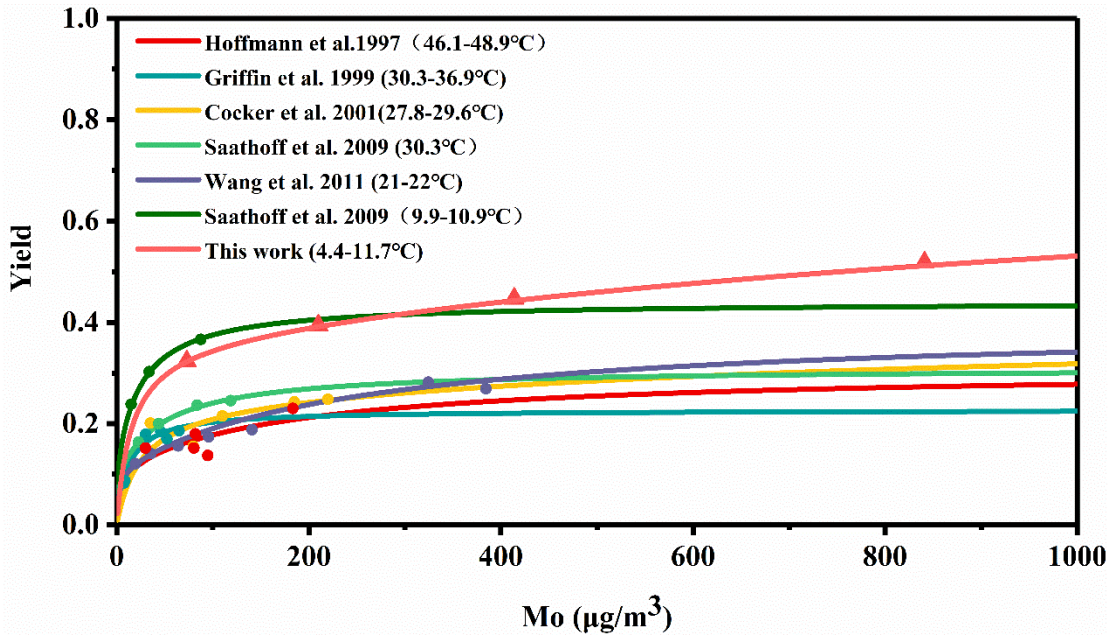

433

434 **Fig. 8.** SOA yield of α-pinene ozonolysis experiments and comparison with other
435 chamber facilities, the unit density (1 g/cm^3) was used for all the experiments when
436 comparing our results with those from previous studies.

437 **3.4.2.2 1,3,5-TMB-NOx photochemical experiments**

438 For 1,3,5-TMB-NO_x photochemical experiments, the density of the formed

aerosols was assumed to be 1.4 g/cm^3 (Nakao et al., 2013), and the details were shown in **Table 5**. In order to obtain the SOA yield more accurately, the vapor wall loss was taken into account. Temperature and seed effect on SOA yield were all considered. As shown in **Table S2**, under same temperature conditions, the presence of seed could reduce timescale associated with reaching gas-particle equilibrium ($\overline{\tau_{g-p}}$), vapor could be more easily partition to the particle phase, and the vapor wall loss could be reduced during the photochemical processes. Under the same seed conditions, temperature increase could reduce the $\overline{\tau_{g-p}}$, and the vapor wall loss would decrease.

As shown in **Table 5**, the SOA yields of 1,3,5-TMB-NO_x was in the range of 4.02-5.43% for high temperature unseeded conditions; when the ammonium sulfate seeds were introduced, the yield was increased (7.08%). Under low temperature unseeded condition, the yield was 8.11%, which was higher than that under high temperature condition; when the ammonium sulfate seeds were introduced, the yield was increased to 11.78%. **Fig. 9** showed the photolysis rate of NO_2 ($J(NO_2)$) of the 1,3,5-TMB-NOx photochemical experiments. The $J(NO_2)$ at high temperature (in summer) was similar, and it was also at low temperature (in winter), but the $J(NO_2)$ in winter was smaller than that in summer. The photolysis rate was positively correlated with the intensity of the photochemical reaction, indicating that the photochemical reaction in winter was weak. However, the SOA yield in winter was higher than that in summer, indicating that temperature was one of the main factors affecting the SOA yield. The results obtained showed that both the temperature and seed could affect the SOA yield, the increase of temperature could lower the SOA yield, while the presence of seed could enhance the SOA yield. Im et al. (2014) reported 1,3,5-TMB SOA yield with the outdoor smog chamber at high temperature unseeded condition, and the yields (4.9±0.4 %, 3.4±0.3 %) were comparable with the data we obtain under similar condition.

According to the vapor wall loss and final SOA yields under various conditions, the seed was suggested to be used in the chamber experiments, as this could minimize the interaction between the gas phase and the chamber walls.

Table 5. Experimental conditions and resulting SOA data of the 1,3,5-TMB

469 photooxidation experiments.

Experiments	Seed	Initial VOC (ppb)	Initial NOx (ppb)	VOC/NO_X (ppbC/ppb)	Temp. (℃)	SOA yield (%)
2019.0903	--	105	211	4.26	24-43	4.02
2019.0925	--	180	197	8.22	24-43	5.43
2019.1014	--	170	250	6.19	12-30	5.21
2019.1025	AS	175	285	4.32	12-28	7.08
2019.1223	--	165	795	1.87	2-17	8.11
2019.1226	AS	167	820	1.83	4-19	11.78
Im et al. (2014)	--	160	243	5.14	17-44	4.9±0.4
Im et al. (2014)	--	165	113	11.12	17-44	3.4±0.3

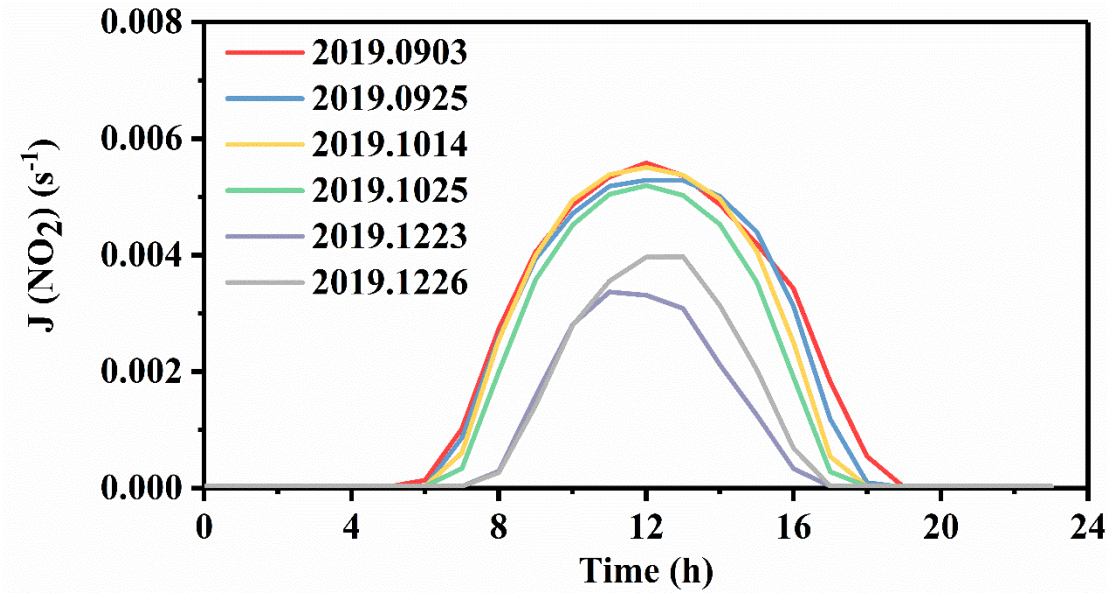

470

471 **Fig. 9** Photolysis rate of NO_2 ($J(NO_2)$) of the 1,3,5-TMB-NO_x photochemical experiments.

472 **4. Conclusions**

473 We have constructed and characterized the CRAES chamber in this study. To our
474 knowledge, it is the only large-scale outdoor chamber in China at present. A series of
475 characterization experiments were performed, including the light transmission of the
476 FEP Teflon film, the mixing ability of the chamber, the background experiments (zero
477 air, zero air +NO_x), and wall loss of gaseous pollutants and particles. The transmission
478 rate was above 90% for the wavelength range 350-900 nm; the mixing time was very
479 short (within 4 min) compared to the entire experimental process (usually several hours);
480 under both zero air and zero air + NO_x background experiments, negligible gases and
481 particles were released from the film or formed; the wall loss rates of propene, ozone,
482 NO, and NO_2 were 0.09×10^{-4}, 2.65×10^{-4}, 0.65×10^{-4}, and 1.01×10^{-4} min^{-1},

respectively; for inorganic ammonium sulfate particles, the wall loss rate was 0.23 h^{-1}, resulting a lifetime of 4.4 h.

The propene-NO_x photo-oxidation reaction was performed and the results were compared with the MCM modelling results, which showed good agreement and meant that it could provide valid data in studying gas-phase photochemistry reactions. For dark reactions, α-pinene-O_3 experiments were performed and two product model was used, the SOA yields fitted well with the model curve. For photochemical reactions, 1,3,5-trimethylbenzene-NO_x experiments were performed, the SOA yields were compared with the data obtained from other chamber facilities. The dark and photochemical reactions showed that temperature and seed could have important effect on the vapor wall loss and SOA yields. Higher temperature and the presence of seed could reduce the vapor wall loss, the seed were suggested to be used in the chamber to reduce the interaction between the gas phase and chamber walls; SOA yield was found to depend inversely on temperature, and the presence of seed could increase SOA yield.

Overall, the results of characterization and preliminary experiments demonstrated that the chamber was in good condition and could be used to provide simulation data with high quality for gas-phase chemistry and secondary air pollutants formation under conditions close to the real atmosphere.

Acknowledgments

This work was supported by China Postdoctoral Science Foundation (2019M660752), Beijing Municipal Science & Technology Commission (No. Z181100005418015), LAC/CMA (2019B08), the Fundamental Research Funds for Central Public Welfare Scientific Research Institutes of China, Chinese Research Academy of Environmental Sciences (No. GYG5051201; No. 2009GGQD18; No. 2019YSKY-018; No. 2019YSKY-012), and Chinese Academy of Sciences Strategic Leading Science and Technology Project (Class B) (XDB05010200). We are very grateful for Prof. Shiro Hatakeyama, Dr.Akinori Takami and Dr. Kei Sato from National Institute of Environment Studies, Japan, and Prof. Xinming Wang from Guangzhou Institute Geochemistry/CAS for their support and assistance during the construction of the smog chamber; we also would like to thank all our colleagues from Chinese Research

Academy of Environmental Sciences, especially Dr. Weiqi Zhang, Dr. Rui Gao, and Dr. Yanjun Ren for their contributions to the construction of the smog chamber. Lastly, we want to show our deep thanks to Mr. Chunshan Liu and his colleagues from Beijing Conway Environmental Technology Co., Ltd. for their helps in building the smog chamber.

Appendix A. Supplementary data

Supplementary data associated with this article can be found in the online version at xxxxxx

References

Akimoto, H., Hoshino, M., Inoue, G., Sakamaki, F., Washida, N., Okuda, M., 1979a. Design and characterization of the evacuable and bakable photochemical smog chamber. Environmental Science and Technology 14, 471-475.

Akimoto, H., Hoshino, M., Inoue, G., Sakamaki, F., Washida, N., Okuda, M., 1979b. Design and characterization of the evacuable and bakable photochemical smog chamber. Environmental science & technology 13, 471-475.

Bloss, C., V.Wagner, Jenkin, M.E., Volkamer, R., Bloss, W.J., Lee, J.D., Heard, D.E., K.Wirtz, Martin-Reviejo, M., Rea, G., C.Wenger, J., Pilling, M.J., 2005. Development of a detailed chemical mechanism (MCMv3.1) for the atmospheric oxidation of aromatic hydrocarbons. Atmospheric Chemistry and Physics 5, 641-664.

Bohn, B., Rohrer, F., Brauers, T., Wahner, A., 2005. Actinometric measurements of NO2 photolysis frequencies in the atmosphere simulation chamber SAPHIR. Atmos. Chem. Phys. 5, 493-503.

Brauers, T., Bohn, B., Johnen, F.-J., Rohrer, F., Bares, S.R., Tillmann, R., Wahner, A., 2003. The atmosphere simulation chamber SAPHIRHE: A tool for the investigation of photochemistry. Geophysical Research Abstracts 5.

CARTER, W.P.L., ATKINSON, R., WINER, A.M., J. N. PITTS, J., 1982a. Experimental investigation of chamber-dependent radical sources. International Journal of Chemical Kinetics 14, 1071-1103.

Carter, W.P.L., Atkinson, R., Winer, A.M., Pitts, J.J.N., 1982b. Experimental investigation of chamber-dependent radical sources. International Journal of Chemical Kinetics 14, 1071-1103.

Chen, T., Liu, Y., Liu, C., Liu, J., Chu, B., He, H., 2019a. Important role of aromatic hydrocarbons in SOA formation from unburned gasoline vapor. Atmospheric Environment 201, 101-109.

Chen, T., Liu, Y., Ma, Q., Chu, B., Zhang, P., Liu, C., Liu, J., He, H., 2019b. Significant source of secondary aerosol: formation from gasoline evaporative emissions in the presence of SO₂ and NH<sub>3</sub&gt. Atmospheric Chemistry and Physics 19, 8063-8081.

Cocker, D.R., Flagan, R.C., Seinfeld, J.H., 2001. State-of-the-art chamber facility for studying atmospheric aerosol chemistry. Environmental science & technology 35, 2594-2601.

Corner, J., Pendlebury, E.D., 1951. The coagulation and deposition of a stirred aerosol. Proceedings of

the Physical Society B, 645-654.
Dodge, M.C., 2000. Chemical oxidant mechanisms for air quality modeling: critical review. Atmospheric Environment 34, 2103-2130.
Donahue, N.M., Henry, K.M., Mentel, T.F., Kiendler-Scharr, A., Spindler, C., Bohn, B., Brauers, T., Dorn, H.P., Fuchs, H., Tillmann, R., Wahner, A., Saathoff, H., Naumann, K.H., Mohler, O., Leisner, T., Muller, L., Reinnig, M.C., Hoffmann, T., Salo, K., Hallquist, M., Frosch, M., Bilde, M., Tritscher, T., Barmet, P., Praplan, A.P., DeCarlo, P.F., Dommen, J., Prevot, A.S., Baltensperger, U., 2012. Aging of biogenic secondary organic aerosol via gas-phase OH radical reactions. Proc Natl Acad Sci U S A 109, 13503-13508.
Griffin, R.J., Cocker, D.R., Flagan, R.C., Seinfeld, J.H., 1999. Organic aerosol formation from the oxidation of biogenic hydrocarbons. Journal of Geophysical Research: Atmospheres 104, 3555-3567.
Grosjean, D., 1985. Wall Loss of Gaseous Pollutants in Outdoor Teflon Chambers. Environmental Science & Technology 19, 1059-1065.
Guo, S., Hu, M., Zamora, M.L., Peng, J., Shang, D., Zheng, J., Du, Z., Wu, Z., Shao, M., Zeng, L., Molina, M.J., Zhang, R., 2014. Elucidating severe urban haze formation in China. Proc Natl Acad Sci U S A 111, 17373-17378.
Hallquist, M., Wenger, J.C., Baltensperger, U., Rudich, Y., Simpson, D., Claeys, M., Dommen, J., Donahue, N.M., George, C., Goldstein, A.H., Hamilton, J.F., Herrmann, H., Hoffmann, T., Iinuma, Y., Jang, M., Jenkin, M.E., Jimenez, J.L., Kiendler-Scharr, A., Maenhaut, W., McFiggans, G., Mentel, T.F., Monod, A., Prevot, A.S.H., Seinfeld, J.H., Surratt, J.D., Szmigielski, R., Wildt, J., 2009. The formation, properties and impact of secondary organic aerosol: current and emerging issues. Atmospheric Chemistry and Physics 9, 5155-5236.
Hess, G.D., Carnovale, F., Copei, M.E., Johnson, G.M., 1992. The evaluation of some photochemical smog reaction mechanisms- ITemperature and initial composition effects. Atmospheric Environment 26A, 625-641.
Hoffmann, T., Odum, J.R., Bowman, F., Collins, D., Klockow, D., Flagan, R.C., Seinfeld, J.H., 1997. Formation of organic aerosols from the oxidation of biogenic hydrocarbons. Journal of Atmospheric Chemistry 26, 189-222.
Huang, R.J., Zhang, Y., Bozzetti, C., Ho, K.F., Cao, J.J., Han, Y., Daellenbach, K.R., Slowik, J.G., Platt, S.M., Canonaco, F., Zotter, P., Wolf, R., Pieber, S.M., Bruns, E.A., Crippa, M., Ciarelli, G., Piazzalunga, A., Schwikowski, M., Abbaszade, G., Schnelle-Kreis, J., Zimmermann, R., An, Z., Szidat, S., Baltensperger, U., El Haddad, I., Prevot, A.S., 2014. High secondary aerosol contribution to particulate pollution during haze events in China. Nature 514, 218-222.
Hurley, M.D., Sokolov, O., Wallington, T.J., 2001. Organic aerosol formation during the atmospheric degradation of toluene. Environmental Science & Technology 35, 1358-1366.
Im, Y., Jang, M., Beardsley, R.L., 2014. Simulation of aromatic SOA formation using the lumping model integrated with explicit gas-phase kinetic mechanisms and aerosol-phase reactions. Atmospheric Chemistry and Physics 14, 4013-4027.
Johnson, D., Jenkin, M.E., Wirtz, K., Martin-Reviejo, M., 2004. Simulating the formation of secondary organic aerosol from the photooxidation of toluene. Environmental Chemistry 1, 150.
Kamens, R.M., Zhang, H., Chen, E.H., Zhou, Y., Parikh, H.M., Wilson, R.L., Galloway, K.E., Rosen, E.P., 2011. Secondary organic aerosol formation from toluene in an atmospheric hydrocarbon mixture: Water and particle seed effects. Atmospheric Environment 45, 2324-2334.

Karl, M., Brauers, T., Dorn, H.P., Holland, F., Komenda, M., Poppe, D., Rohrer, F., Rupp, L., Schaub, A., Wahner, A., 2004. Kinetic Study of the OH-isoprene and O3-isoprene reaction in the atmosphere simulation chamber, SAPHIR. Geophysical Research Letters 31, n/a-n/a.

Kelly, N.A., 1982. Characterization of Fluorocarbon-Film Bags as Smog Chambers. Environmental Science and Technology 16, 763-770.

Knox, J.H., 1965. A New Mechanism for the Low Temperature Oxidation of Hydrocarbons in the Gas Phase. Combustion and Flame 9, 297-310.

Leone, J.A., Flagan, R.C., Geosjean, D., Seinfeld, J.H., 1985. An outdoor smog chamber and modeling study of Toluene-NO Photooxidation. International Journal of Chemical Kinetics 17, 177-216.

Li, J., Li, K., Wang, W., Wang, J., Peng, C., Ge, M., 2017a. Optical properties of secondary organic aerosols derived from long-chain alkanes under various NO x and seed conditions. Science of The Total Environment 579, 1699-1705.

Li, J., Wang, W., Li, K., Zhang, W., Peng, C., Zhou, L., Shi, B., Chen, Y., Liu, M., Li, H., Ge, M., 2020. Temperature effects on optical properties and chemical composition of secondary organic aerosol derived from n-dodecane. Atmospheric Chemistry and Physics 20, 8123-8137.

Li, K., Chen, L., White, S.J., Yu, H., Wu, X., Gao, X., Azzi, M., Cen, K., 2018a. Smog chamber study of the role of NH 3 in new particle formation from photo-oxidation of aromatic hydrocarbons. Science of The Total Environment 619-620, 927-937.

Li, K., Li, J., Liggio, J., Wang, W., Ge, M., Liu, Q., Guo, Y., Tong, S., Li, J., Peng, C., Jing, B., Wang, D., Fu, P., 2017b. Enhanced Light Scattering of Secondary Organic Aerosols by Multiphase Reactions. Environmental science & technology 51, 1285-1292.

Li, K., Li, J., Wang, W., Li, J., Peng, C., Wang, D., Ge, M., 2018b. Effects of Gas-Particle Partitioning on Refractive Index and Chemical Composition of m-Xylene Secondary Organic Aerosol. J Phys Chem A.

Liu, S., Jia, L., Xu, Y., Tsona, N.T., Ge, S., Du, L., 2017. Photooxidation of cyclohexene in the presence of SO2: SOA yield and chemical composition. Atmospheric Chemistry and Physics 17, 13329-13343.

Ma, Q., Lin, X., Yang, C., Long, B., Gai, Y., Zhang, W., 2018. The influences of ammonia on aerosol formation in the ozonolysis of styrene: roles of Criegee intermediate reactions. Royal Society Open Science 5, 1-12.

Martian-Reviejo, M., Wirtz, K., 2005. Is Benzene a Precursor for Secondary Organic Aerosol? Environmental Science and Technology 39, 1045-1054.

McFiggans, G., Mentel, T.F., Wildt, J., Pullinen, I., Kang, S., Kleist, E., Schmitt, S., Springer, M., Tillmann, R., Wu, C., Zhao, D., Hallquist, M., Faxon, C., Le Breton, M., Hallquist, A.M., Simpson, D., Bergstrom, R., Jenkin, M.E., Ehn, M., Thornton, J.A., Alfarra, M.R., Bannan, T.J., Percival, C.J., Priestley, M., Topping, D., Kiendler-Scharr, A., 2019. Secondary organic aerosol reduced by mixture of atmospheric vapours. Nature 565, 587-593.

McMurry, P.H., Grosjean, D., 1985. Gas and aerosol wall losses in Teflon film smog chambers. . Environmental science & technology 19, 1176-1182.

Menon, S., Hansen, J., Nazarenko, L., Luo, Y.F., 2002. Climate effects of black carbon aerosols in China and India. Science 297, 2250-2253.

Metzger, A., Dommen, J., Gaeggeler, K., Duplissy, J., Prevot, A.S.H., Kleffmann, J., Elshorbany, Y., A.Wisthaler, Baltensperger, U., 2008. Evaluation of 1,3,5 trimethylbenzene degradation in the detailed tropospheric chemistry mechanism, MCMv3.1, using environmental chamber data.

Atmosphere Chemistry and Physics 8, 6453-6468.
Nakao, S., Tang, P., Tang, X., Clark, C.H., Qi, L., Seo, E., Asa-Awuku, A., Cocker, D., 2013. Density and elemental ratios of secondary organic aerosol: Application of a density prediction method. Atmospheric Environment 68, 273-277.
Odum, J.R., Hoffmann, T., Bowman, F., Collins, D., Flagan, R.C., Seinfeld, J.H., 1996. Gas/particle partitioning and secondary organic aerosol yields. Environmental science & technology 30, 2580-2585.
Paulsen, D., Dommen, J., Kalberer, M., Preavot, A.S.H., Richter, R., Sax, M., Steinbacher, M., Weingartner, E., Baltensperger, U., 2005a. Secondary organic aerosol formation by irradiation of 1,3,5-Trimethylbenzene-NOx-H2O in a new reaction chamber for atmospheric chemistry and physics. Environmental Science & Technology 39, 2668-2678.
Paulsen, D., Dommen, J., Kalberer, M., Prevot, A.S.h., Richter, R., Sax, M., Steinbacher, M., Weingartner, E., Baltensperger, U., 2005b. Secondary organic aerosol formation by irradiation of 1,3,5-trimethylbenzene-NOx-H2O in a new reaction chamber for atmospheric chemistry and physics. Environmental Science and Technology 39, 2668-2678.
Peng, C., Wang, W., Li, K., Li, J., Zhou, L., Wang, L., Ge, M., 2018. The optical properties of limonene secondary organic aerosols: the role of NO3, OH and O3 in the oxidation processes. Journal of Geophysical Research: Atmospheres.
Poschl, U., Shiraiwa, M., 2015. Multiphase Chemistry at the Atmosphere-Biosphere Interface Influencing Climate and Public Health in the Anthropocene. Chem. Rev. 115, 4440-4475.
Ren, Y., Bernard, F., Daele, V., Mellouki, A., 2019. Atmospheric fate and impact of perfluorinated butanone and pentanone. Environmental science & technology 53, 8862-8871.
Ren, Y., Grosselin, B., Daele, V., Mellouki, A., 2017. Investigation of the reaction of ozone with isoprene, methacrolein and methyl vinyl ketone using the HELIOS chamber. Faraday Discuss 200, 289-311.
Rohrer, F., Bohn, B., Brauers, T., Bruning, D., Johnen, F.-J., Wahner, A., Kleffmann, J., 2005. Characterisation of the photolytic HONO-source in the atmosphere simulation chamber SAPHIR. Atmos. Chem. Phys. 5, 2189-2201.
Rollins, A.W., Kiendler-Scharr, A., Fry, J.L., Brauers, T., Brown, S.S., Dorn, H.-P., Dube, W.P., Fuchs, H., Mensah, A., Mentel, T.F., Rohrer, F., Tillmann, R., Wegener, R., Wooldridge, P.J., Cohen, R.C., 2009. Isoprene oxidation by nitrate radical: alkyl nitrate and secondary organic aerosol yields. Atmosperic Chemistry and Physics 9, 6685-6703.
Saathoff, H., Naumann, K.-H., Mo¨hler, O., Jonsson, A.M., Hallquist, M., Kiendler-Scharr, A., Mentel, T.F., Tillmann, R., Schurath1, U., 2009. Temperature dependence of yields of secondary organic aerosols from the ozonolysis of α-pinene and limonene. Atmosperic Chemistry and Physics 9, 1551-1577.
Seakins, P.W., 2010. A brief review of the use of environmental chambers for gas phase studies of kinetics, chemical mechanisms and characterisation of field instruments. EPJ Web of Conferences 9, 143-163.
Simonaitis, R., Meagher, J.F., Bailey, E.M., 1997. Evaluation of the condensed carbon bond (CB-IV) mechanism against smog chamber data at low VOC and NOx concentrations. Atmospheric Environment 31, 27-43.
Tang, X., Bi, M., Li, J., Zhang, X., 1982. Trial production and performance experiment of photochemical smog chamber. Environmental Chemistry 1, 344-351.
Wang, W.-G., Li, K., Zhou, L., Ge, M.-F., Hou, S.-Q., Tong, S.-R., Mu, Y.-J., Jia, L., 2015. Evaluation

and Application of Dual-Reactor Chamber for Studying Atmospheric Oxidation Processes and Mechanisms. Acta Physico-Chimica Sinica 31, 1251-1259.

Wang, X., Liu, T., Bernard, F., Ding, X., Wen, S., Zhang, Y., Zhang, Z., He, Q., Lu, S., Chen, J., Saunders, S., Yu, J., 2014. Design and characterization of a smog chamber for studying gas-phase chemical mechanisms and aerosol formation. Atmospheric Measurement Techniques 7, 301-313.

Warneke, C., de Gouw, J.A., Goldan, P.D., Kuster, W.C., Williams, E.J., Lerner, B.M., Jakoubek, R., Brown, S.S., Stark, H., Aldener, M., Ravishankara, A.R., Roberts, J.M., Marchewka, M., Bertman, S., Sueper, D.T., McKeen, S.A., Meagher, J.F., Fehsenfeld, F.C., 2004. Comparison of daytime and nighttime oxidation of biogenic and anthropogenic VOCs along the New England coast in summer during New England Air Quality Study 2002. Journal of Geophysical Research-Atmospheres 109.

Wirtz, K., Martin-Reviejo, M., 2003. Density of secondary organic aerosols. J. Aerosol Sci. 34, S223–S224.

Wu, S., Lu, Z., Hao, J., Zhao, Z., Li, J., Takekawa, H., Minoura, H., Yasuda, A., 2007. Construction and characterization of an atmospheric simulation smog chamber. Advances in Atmospheric Sciences 24, 250-258.

Yu, J., Jeffries, H.E., Sexton, K.G., 1997. Atmospheric photooxidation of alkylbenzenes- Ⅰ. carbonyl product analyses. Atmospheric Environment 31, 2261-2280.

Zador, J., Wagner, V., Wirtz, K., Pilling, M., 2005. Quantitative assessment of uncertainties for a model of tropospheric ethene oxidation using the European Photoreactor (EUPHORE). Atmospheric Environment 39, 2805-2817.

Zhang, H., Hu, D., Chen, J., Ye, X., Wang, S.X., Hao, J.M., Wang, L., Zhang, R., An, Z., 2011. Particle Size Distribution and Polycyclic Aromatic Hydrocarbons Emissions from Agricultural Crop Residue Burning. Environmental science & technology 45, 5477-5482.

Zhang, H., Wang, S., Hao, J., Wang, X., Wang, S., Chai, F., Li, M., 2016. Air pollution and control action in Beijing. Journal of Cleaner Production 112, 1519-1527.

Zhang, W., Wang, W., Li, J., Peng, C., Li, K., Zhou, L., Shi, B., Chen, Y., Liu, M., Ge, M., 2020. Effects of SO2 on optical properties of secondary organic aerosol generated from photooxidation of toluene under different relative humidity. Atmospheric Chemistry and Physics 20, 4477–4492.

Zhang, Y., Li, J., 1998. Research on photochemical smog pollution in Chinese cities. Acta Scientiarum Naturalium Universitatis Pekinensis 34, 392-400.

Zhou, C., Jang, M., Yu, Z., 2019. Simulation of SOA formation from the photooxidation of monoalkylbenzenes in the presence of aqueous aerosols containing electrolytes under various NOx levels. Atmospheric Chemistry and Physics 19, 5719-5735.